Gate-tunable atomically-thin lateral MoS_2 Schottky junction patterned by electron beam

Y. Katagiri[1], T. Nakamura[2], A. Ishii[3], C. Ohata[1], M. Hasegawa[3], Y. K. Fukai[1], S. Katsumoto[2], T. Cusati[4], A. Fortunelli[5], G. Iannaccone[4], G. Fiori[4], S.Roche[6,7], J. Haruyama[1]

[1]Department of Electrical Engineering and Electronics, and [3]Chemistry and Biological Science, Aoyama Gakuin University, 5-10-1 Fuchinobe, Sagamihara, Kanagawa 252-5258, Japan
[2] Institute for Solid State Physics, The University of Tokyo, 5-1-5 Kashiwanoha, Kashiwa, Chiba 277-8581, Japan
[4] Dipartimento di Ingegneria dell'Informazione. Università di Pisa, Via G. Caruso, 16 Pisa 56122, Italy
[5] CNR-ICCOM, via Giuseppe Moruzzi 1, 56124, Pisa, Italy
[6] Catalan Institute of Nanoscience and Nanotechnology (ICN2), CSIC and The Barcelona Institute of Science and Technology, Campus UAB, Bellaterra, 08193 Barcelona, Spain
[7] ICREA, Institució Catalana de Recerca i Estudis Avançats, 08070 Barcelona, Spain

Among atomically-thin two-dimensional (2D) materials, molybdenum disulphide (MoS_2) is attracting considerable attention because of its direct bandgap in the 2H-semiconducting phase. On the other hand, a 1T-metallic phase has been revealed, bringing complementary application. Recently, thanks to top-down fabrication using electron beam (EB) irradiation techniques, in-plane 1T-metal/2H-semiconductor lateral (Schottky) MoS_2 junctions were demonstrated , opening a path towards the co-integration of active and passive two-dimensional devices. Here, we report the first transport measurements evidencing the formation of a MoS_2 SB junction with barrier height of 0.13 ~ 0.18 eV created at the interface between EB-irradiated (1T)/non-irradiated(2H) regions. Our findings supported by state-of-the-art dive simulation reveal that the barrier height is highly sensitive to electrostatic charge doping and almost free from Fermi level pinning, a fact unique to atom-thin 1T layers, and a fingerprint of Schottky barrier-based field-effect transistors

MoS_2, one of the transition metal dichalcogenides, is much attractive among atomically-thin 2D materials[1-26], because of its direct bandgap of 1.5 ~ 1.8 eV in 2H semiconducting phase, especially when atom-thin or flexible circuitry is required. On the other hand, the 1T-metallic phase, engineered by chemical doping and laser-beam irradiation, is also useful for some application such as ohmic metallic junction between metal electrode and 2H-MoS_2, and supercapacitor electrode with capacitance value as high as ~700 F/cm^3 [14-19,21]. An electronic transition from the 2H (trigonal prismatic D3h) semiconducting to the 1T (octahedral Oh) metal phases of MoS_2 triggered by EB irradiation (see Fig. 2E) has been recently observed under the in-situ transmission electron microscope (TEM) at high substrate temperature[12]. The two phases can easily be converted from one to the other via intralayer atomic plane gliding, which involves a transversal displacement of one of the *S* planes (Fig. 2E), caused by the charge accumulation and direct momentum transfer from EB combined with substrate heating.

However, to date, such structural observations have not been harnessed to fabricate practical in-plane lateral Schottky junctions and SB devices. It is even unclear whether such lateral SB can be actually formed within atomically thin layers only through atomic-order phase transition. Moreover, if SB devices fabricated with graphene have been already reported, they have been realized with vertically stacked hetero-structures via van der Waals engineering and metal/MoS_2 interfacing, which are not suitable for large scale integration[34-37]. The EB-irradiated top-down fabrication of in-plane 1T/2H Schottky junctions[27-30] and SB field effect transistors (SB-FET)[31-33] is highly important, because the EB-patterned technique could be in principle scalable to large complex in-plane circuitry. Here, we fabricate this atomically thin EB-patterned lateral MoS_2 Schottky junctions and SB-FET. The device characteristics (with confirmation by X-ray photoelectron spectroscopy (XPS), Raman[14-20] and photoluminescence (PL) spectroscopies), highlighted by rectification and SB-FET[27-33] properties and supported by first-principles simulations[38-40], reveal the formation of 2D SBs[30], which have high tunability by gate-electrostatic-induced doping (0.13 ~ 0 eV for back-gate voltage (V_{bg}) of 0 ~ 4V) and are free from Fermi level (E_F) pinning, a fact unique to atomically thin layers with low charge-carrier capability.

In order to create 1T phase embedded into 2H phase, few layer *n*-type MoS_2 flakes with thickness ~8 nm (~7 layers) have been fabricated by mechanical exfoliation of bulk MoS_2 following scotch tape method (Fig. 1A). Two regions on one sample with individual area of 1.5 $\times$ 1 μm^2 have been exposed to EB irradiation with different doses (Fig. 1A; 100 Me/nm^2 for region 1 and 160 Me/nm^2 for region 2), without using any dopant at room temperature (see supplementary materials (SM) 1). This was followed by the patterning of two Au/Ti (500nm/20nm thick) electrode pairs on individual

regions (Fig. 1B). Electrode pair 1-2 is contacted to non-EB-irradiated bulk, while, in the electrode pair 3-4, one electrode is contacted to EB irradiated and the other to non-EB-irradiated bulk. From here on, we will refer to the fabricated device on regions 1 and 2 as Devices 1 and 2, respectively. Back gate electrode was also attached on the back-side of Si substrate with thick SiO_2 layer (~300 nm).

Figures 1C and 1D show XPS spectra of the sample shown in Fig. 1A, measured including the EB- irradiated region 2 and non-irradiated region (see SM2). The figures show the characteristic Mo 3*d*, S 2*s* (Fig. 1C), and S 2*p* (Fig. 1D) peaks of the 1T phases of MoS_2[14,15], although the larger area of 2H phase results in higher intensity. Typical Raman spectra for EB-irradiated region 2 are also given in Fig. 1E. We observe two weak but distinct peaks (i.e., J_1 and J_2 around 150 and 216 cm^{-1}, respectively). These peak positions are in good agreement with previous reports of Raman spectrum for 1T phase MoS_2[16-20]. Region 1 does not exhibit such peaks. PL map (inset) and spectra measured at selected four points (main panel) are also reported in Fig. 1F(see SM3). Two prominent absorption peaks are clearly identified at ~670 and ~627 nm in the spectra (No, 1-3), which agrees with previous PL reports of 2H-MoS_2 with thickness similar to the present samples[20], and its entire elimination (No. 4) on EB non-irradiated and irradiated regions, respectively. These results strongly suggest the formation of metal (1T) and semiconductor (2H) phases in the EB-irradiated region 2 and non-irradiated region, respectively. The observed 1T phase is stable even after one month in contradiction to ref. 41. One of the possible reasons might be that in our samples, the 1T phase is not free standing but embedded into 2H phase.

Figure 2 shows the current (I) *vs* voltage (V) for two measured devices. Device 1 exhibits a symmetric characteristics for both electrode pairs, with non-negligible current in correspondence of V = ±1.5V (Fig. 2A), as expected for conventional metal-semiconductor-metal structures (i.e., (Au/Ti)/bulk 2H-MoS_2/(Au/Ti) in Fig. 1E)[28]. This suggests that the EB-irradiated region in Device 1 does not show any metallic transition and keeps an electronic fingerprint qualitatively similar to bulk MoS_2.The EB dose of 100 Me/nm^2 applied to region 1 is too weak to provoke a phase transition. We estimate that the forward voltage (V_F) of our Schottky junction (Au/Ti)/2H-MoS_2 is about ~2V in Fig. 2A (V_F is the voltage at which forward current attains to 4.5 A).

In contrast, I_{34} *vs* V_{34} characteristics for electrode pair 3-4 of Device 2 strongly differ from those of Device 1 (Fig. 2B). Remarkably, a clear asymmetric behavior (i.e., rectification property) is observed with an onset bias voltage of ~+2.5 V. Such an asymmetric electrical feature can be clearly related to the formation of a Schottky junction[27], with a barrier height seen by electrons different with respect to that seen by holes. As mentioned above, XPS, Raman, and PL spectra suggest the formation of 1T-phase in EB-irradiated region 2. Because 1T-phase is metallic, the observed Schottky behavior can be explained by the formation of a metal-(1T-phase)/semiconductor(bulk 2H) in-plane junction at the surface within ~3 layers (Fig. 2D). Indeed, an electrode pair contacted to a region irradiated by an EB with dose of 160 Me/nm^2 in another sample (Device 2') actually exhibits a metallic characteristic (i.e., a symmetric behavior showing no rectification property) (Fig. 2C). Moreover, electrode pair 1-2 of Device 2 does not drive any current (i.e., $I_{12} < \pm 200$nA at $V_{12} < \pm 5$V). This supports the presence of two Schottky junctions with large barrier heights between electrodes 1 and 2 in Device 2 (Fig. 2E), because reverse bias voltage regime for applied V_{12} (i.e., corresponding to $-V_{34}$ regime of Device 2 in Fig. 2B) is dominant for the symmetrically placed two Schottky junctions. In Fig.2B, V_F is as large as ~5V. This is much larger than V_F = 2V of the (Au/Ti)/2H-MoS_2 junction shown in Fig. 2A. SinceV_F is basically proportional to Schottky barrier height, the Schottky barrier height for Fig. 2B is thus different as compared that of Au/Ti/2H-MoS_2 junction and, hence, the Schottky barrier for Fig. 2B is attributed to 2H/1T phase junction. From these V_F values, the barrier height of (Au/Ti)/2H phase is estimated to be as small as 0.05eV ~0.07eV, whereas that for 2H/1T is 0.13 ~ 0.18 eV.

Next, we focus on the electrical characteristics of electrode pair 3-4 in Device 2, as a function of V_{34} for different V_{bg} (Fig. 1E). Figure 3A shows a typical logarithmic I_{34} *vs* V_{bg} characteristics for V_{34} = +1V (i.e., forward bias voltage region). Under $+V_{bg}$, these characteristics resemble that of a n-type SB-FET[31-33], which consists of (1T-MoS_2 metal)/2H-MoS_2 n-semiconductor/(Ti/Au electrode) (Fig. 3C). As $+V_{bg}$ increases, the barrier at the Schottky contacts is thinned, and electrons can easily flow from the right contact to the channel and eventually to the left contact, increasing I_{34}. As it can be seen in Fig. 3A, the current is modulated over 4 orders of magnitude ($I_{on}/I_{off} \sim 10^4$) and the subthreshold slope (*SS*) is approximately 1 V/decade. The obtained *SS* is almost the same as that observed in CNT-SB-FET and SB-MOSFET with SB height of 0.3 eV and thick back gate oxide[32,33]. This also supports the formation of a SB in Device 2.

Figure 3B shows I_{34} *vs* V_{bg} characteristics for reverse biasing (i.e., V_{34} = -1V and -3V). For this biasing, electrons accumulate in 1T-MoS_2 metal reservoir, leading to an increase of the E_F (Fig. 3D, where eV_{accum} is the electrostatic energy due to electron accumulation). This effect is responsible for a small leakage current of Schottky junction (i.e., $-I_{34}$) due to thermionic emission of electrons (Fig. 3D). At V_{34} = -3V, E_F in 1T-metal region locates at higher energy and energy difference between E_F and the top of Schottky junction is small compared to V_{34} = -1 V. Thus, $-I_{34}$ values are larger.

Figs. 4A – 4C show Arrhenius plot for I_{34} normalized over temperature (i.e., $I_{34}/T^{3/2}$ for 2D Schottky junction formula given by eqs. (1 -4)) for different V_{bg} (V_{bg} = 0V, 4V, and 2V, respectively) and fixed V_{34} = -2V (i.e., reverse bias). For Fig. 4A, I_{34} linearly decreases below $1/T_c$ = ~0.0067 as 1/T value increases (*i.e.*, I_{34} increases at critical T (T_c) > 150K with increasing T), while I_{34} significantly drops above $1/T_c$. In contrast, in Fig. 4B, for 1/T smaller than $1/T_c$ (*i.e.*, high T), the curve becomes constant (i.e., T-independent). This can be explained by the fact that for large V_{bg}, the SB becomes almost transparent and thermal energy does not significantly contribute to increase I_{34} (as explained for Figs. 4D, 4E, and 5E later).

The experimental data (Figs. 4A and 4B) are analyzed using the expression of the current (I) in a 2D Schottky diode as a function of T[30].

$$I = I_{2D}\left[\exp\left(qV/\eta k_B T\right) - 1\right] \quad (1)$$

$$I_{2D} = W A^*_{2D} T^{\frac{3}{2}} \exp\left(-\frac{q\phi_B}{k_B T}\right) \quad (2)$$

$$A^*_{2D} = q\sqrt{8\pi k_B^2 m^*}/h^2 \quad (3)$$

$$m^* = 0.45 m_0 \quad (4)$$

where η is the diode ideality factor (i.e., takes into account the presence of generation/recombination phenomena), A_{2D}* is the 2D Richardson constant, W (=1.5μm) is the junction length, Φ_B is the SB height, k_B is the Boltzmann constant, m* is the effective mass of MoS_2, and m_0 is the mass of electron. When a negative V_{SD} (corresponding to $-V_{34}$ in our device) is applied, eq. (1) results in $I = -I_{2D}$. Thus, the T-dependence of I_{SD} agrees with the T-dependence given by eq. (2).

The linear relationships obtained in Figs. 4a and 4b support the validity of eq. (2) describing the formation of a Schottky junction at the interface between EB-irradiated/non-irradiated (bulk) regions of Device 2. The best fits using eqs. (2) - (4) (dotted lines) give Φ_{B1} ~ 0.13 eV at 1/T < 0.0067 K^{-1} and Φ_{B2} ~ 0.18 eV at 1/T > 0.0067 K^{-1} in Fig. 4A, and Φ_{B3} ~ 0.15 eV at 1/T > 0.0067 K^{-1} in Fig. 4b, when total area of the Schottky junction S = 2,500 nm^2, and η = 1.07 are used. The result η = 1.07 suggests the presence of generation/recombination current at the junction, possibly owing to defects introduced by the EB irradiation.

For Fig. 4A, the origin of two SB with heigths Φ_B estimated at temperatures above and below T_c can be understood from the obtained two S values, which give the best fits. Φ_{B1} ~ 0.13 eV at 1/T < 0.0067 and Φ_{B2} ~ 0.18 eV at 1/T > 0.0067 give S = 5 nm × 300 nm and 5 nm ×200 nm, respectively. For Fig. 4B, an interesting T-independent Φ_B ~ 0 eV at 1/T < 0.0067 K^{-1} is observed. Figure 4C exhibits a result at intermediate V_{bg} (= +2V) between Fig. 4A (V_{bg} = 0) and 4b (V_{bg} = +4V). Φ_B ~ 0.015 eV at 1/T < 0.0067 K^{-1} actually corresponds to intermediate value. Including these results, Fig. 4D reveals the high sensitivity of Φ_B to applied V_{bg}, implying highly gate-tunable Φ_B. The origin is explained in the later part, based on Figs. 4E, and 5E.

To deepen the analysis of the 2H/1T interface, we have performed DFT calculations, considering the geometry of 2H/1T MoS_2 interfaces as experimentally observed with atomistic details given in [12]. This approach allows us to obtain accurate information on the SB forming at the 2H/1T interface, taking into account both the band offset and the formation of dipoles. We neglect the possible contribution of interface defects or recombination centers, which are likely present (suggested experimentally by the Schottky factor η = 1.07, which is larger than 1) and can provide localized states affecting the SB. First-principles DFT calculations are performed using the Quantum Espresso package[38], utilizing a plane wave basis set, a gradient-corrected exchange-correlation functional[39], and scalar-relativistic ultrasoft pseudopotentials (US-PPs)[40] (SM4). Figs. 5A and 5B show the computed bands for monolayer 1T and 2H-phase MoS_2, respectively. Exploiting the information in [12], we built a periodic model of a 2H/1T/2H heterojunction whose atomistic structure is shown in Figs. 5C, 5D, and which represents a realistic model of a 1T-phase embedded within the generating 2H phase.

Figure 5E shows a plot of the vacuum level potential profile with respect to E_F showing the formation of dipoles at the hetero-interfaces. DFT calculations provide a value of 0.73 eV for the energy difference between the electron affinity of 2H MoS_2 and the work function of 1T MoS_2. From this information, we plot in Figure 5F the conduction band edge profile in the structure relative to the E_F, and extract a Φ_B of 0.47 eV, in reasonably good agreement with the experimental results. The residual discrepancy between predicted and observed values of the Shottky barrier can be ascribed to several effects. One likely effect is the change in the work function of the 1T phase due to doping by the contact electrode: indeed, from test calculations we found that such a doping induces an upward shift in the background potential of the 1T phase by ≈0.3-0.4

eV which could easily account for the observed discrepancy. Other possibilities include the mentioned defects and recombination centers at the interface which can induce mid-gap states, thus reducing the effective Φ_B. Indeed, a dependence of the Shottky barrier on the work function has been observed in other Schottky junctions: for example the Φ_B of non-hydrogenated and hydrogenated Pd/few-layer MoS_2 SBs were reported to be 0.25 eV and 0.15 eV, respectively. Hydrogenation of Pd reduced the work function of Pd and subsequently reduced the Φ_B to ~0.1 eV[31]. Moreover, a value of 0.3 eV for Φ_B was reported in SB-MOSFET with *S* value (~1V/decade) similar to ours as mentioned above[32].

One can also see in Fig. 5E that the potential in the 1T phase shows some variations at the interface, because 1T MoS_2 has a relatively low density of states (in this sense it is not an ideal metal). This also explains the observed highly V_{bg}-sensitive Φ_B (Fig. 4D). As the V_{bg} is increased, electrons doped from substrate accumulate in the 1T-phase region under $-V_{34}$, increasing E_F with respect to the conduction band (Fig. 4E; $-e(V_{34}+ V_{accm})$), hence decreasing Φ_B to Φ_B'. When E_F in the 1T-metal region coincides with the top of the Schottky junction by further increasing V_{bg}, Φ_B' becomes zero and, thus, electrons feel no SB. Therefore, a T-independent zero-Φ_B value appears. The dependence of Φ_B on T is likely to depend on the energy and nature of localized states at the hetero-interface. This tunable Fermi level E_F, highly sensitive to electrostatic carrier doping via. back-gate electrode, is unique to the present SB consisting of 1T phase of atomically thin (~3 layers) MoS_2. It also implies that the E_F is almost free from pinning by defects at the SB despite of the presence of generation/recombination center, particularly in the high T regime. This is also a significant benefit of the atomically thin layers, in which pinned E_F can be easily shifted by increased electro-static potentials induced by the accumulation of the doped charge carriers in 1T area. This high tunability can be highly useful in future atomically-thin in-plane device applications.

In conclusion, we demonstrated the first EB-patterned gate-tunable in-plane atomically-thin Schottky junction and SB-FET fabricated with a top-down approach, by inducing a structural phase change in few-layer MoS_2 through an EB irradiation dose of 160 Me/nm^2 at room temperature. Observation of XPS, Raman, and PL spectra exhibit presence of 1T metallic phase on the EB irradiated region. Experimental measurements and ab-initio simulations provide a coherent physical picture of the properties of the 2D Schottky junction created at the interface of EB-irradiated (1T) /non-irradiated (2H) regions. The difference between the experimentally observed SB height (~0.13 - 0.18 eV) and the one obtained by theory (0.47 eV) highlight the presence of defects and recombination centers introduced by EB irradiation. Electrostatic-induced carrier doping by V_{bg} enables tuning the SB height due to low density of states of 1T phase (0.13 ~ 0 eV for V_{bg} of 0 ~ 4V), resulting in the T-independent zero-SB height. This EB top-down patterning opens the possibility to fabricate in-plane lateral heterostructure FETs[9], which have shown promising scaling prospects in the nm range[10], and/or local interconnects directly with metallic phase (1T) between (2H)MoS_2 transistors, resulting in ultimate flexible and wearable in-plane integration circuits without using 3D metal wirings. After this initial work, more efforts are needed to mitigate the presence of interface defects and to establish the atomic-scale in-plane SB devices as building blocks of 2D electronic and optoelectronic circuits.

Author information

Corresponding author: E-mail J-haru@ee.aoyama.ac.jp

Author contributions

Y. K., T. N., A. I., C. O., and Y.K.F. performed experiments. T.C., A. F., G.I. and G. F. performed theoretical calculation. J. H., S. K., T. N., M. H. designed the experiments. J.H. and A.I. analyzed the data. J. H., T.C., A.F., S.R., G. I., and G. F.

Notes

The authors declare no competing financial interest.

Acknowledgements

The authors thank T. Enoki, S. Tarucha and T. Ando for their technical contribution, fruitful discussions, and encouragement. This work at Aoyama Gakuin was partly supported by a Grant-in-aid for Scientific Research (Basic research A: 24241046) and grant for private University in MEXT and AOARD grant (135049) in U.S. Air Force Office of

Scientific Research. The Tokyo University's work was also supported by the Special Coordination Funds for Promoting Science and Technology. Computational resources at nanohub.org are gratefully acknowledged. S. Roche acknowledges support from the Severo Ochoa Program (MINECO, Grant No. SEV-2013-0295). G.Iannacconne,Gianluca Fiori and Stephan Roche acknowledge the funding from the European Union Seventh Framework Programme under Grant agreement No. 604391 Graphene Flagship.

References

1. Novoselov, K. S. *et al., Science.* 2004, **306**, 666.
2. Geim, A. K. & Grigorieva, I. V. V, *Nature.* 2013, **499**, 419–425.
3. Roy, T. *et al., ACS Nano.* 2014, **8**, 6259.
4. Li, L. *et al., Nature Nanotech*. 2014, **9**, 372.
5. Herrero, P.-J. *et al., Nature Nanotech*. 2014, **9**, 330.
6. Ferrari, A. C., Bonaccorso, F., Falko, V., Novoselov, K.S., Roche, S. *et al., Nanoscale*. 2015, **7**, 4598-4810.
7. Kang, K., Xie, S., Huang, Li., Han, Y., Huang, P.Y., Fai Mak, K., Kim, *et. al., Nature.* 2015, **520**, 656.
8. Fiori, G., Iannaccone, G., Palacios, T., et al, *Nature Nanotech.* 2014, **9**,768–779.
9. Fiori, G., Betti, A., Bruzzone, S., Iannaccone, G., *ACS NANO.* 2012, **6**, 2642-2648.
10. Logoteta, D., Fiori, G., Iannaccone, G., *Scientific Reports.* 2014, **4** (6607), 1-6.
11. Levendorf, M.P., Kim, C. –J., Brown, L., et al, *Nature*. 2012, **488**, 627–632.
12. Lin, Y.-C., Suenaga, K. et al., *Nature Nanotech.* 2014, **9**, 391-396.
13. Eda, G. *et al.*, *ACS Nano.* 2012, **6**, 7311–7317.
14. Acerce, M. *et al*., *Nature Nanotechnology*. 2015, **10**, 313-318.
15. Kappera, R. *et al.*, *Nature Materials.* 2014, **13**, 1128-1134.
16. Jiang, L., Zeng, H. *et al*. *Mater. Res. Lett.*, 2015, **3(4)**, 177–183.
17. Guo, Y., Heinz, T. F. *et al*. *Nano Lett.* 2015, DOI: 10.1021/5b01196.
18. Nayak, A. P., Akinwande, D. *et al. Nano Lett.* 2014, DOI/10.1021/nl5036397.
19. Liu, Q., Song, L. *et al., Small.* 2015, **11***,* No. 41, 5556–5564.
20. Splendani, A. *et al.*, *Nano Lett.* 2010, **10,** 1271–1275.
21. Cho, S. *et al*., *Science.* 2015, **349**, 625-628.
22. Lee, C.-H. *et al.*, *Nature Nanotech.* 2014, **9**, 676-681
23. Hong, X., Kim, J. *et al.*, *Nature Nanotech*. 2014, **9**, 682.
24. Choi, M. S. *et al.*, *Nature Commun.* 2013, **4**, 1624.
25. Wang, H. *et al., Nano Lett.* 2012, **12**, 4674.
26. Radisavljevic, B., Radenovic, A., Brivio, J., Giacometti, V. & Kis, A. *Nature Nanotech.* 2011, **6**, 147–150.
27. Sze, S. M. & Ng, K. K. Physics of Semiconductor Devices. 2006, 3rd edn (Wiley).
28. Fontana, M. *et al. Scientific Reports.* 2013, **3**, 1634.
29. Lince, J. R., Carre, D. J. & Fleischauer, P. D. *Phys. Rev.* **B.** 1987, **36**, 1647–1656.
30. Anwar, A., Nabet, B., Culp, J., and Castro, F., *J. Appl. Phys.* 1999, **85**, 2663.
31. Dai, H. *et al*., *Nature.* 2003, **424**, 654.
32. Appenzeller, J. *et al*., *Phys. Rev. Lett.* 2002, **89**, 126801.
33. Heinze, H. *et al.*, *Phys. Rev. Lett*. 2002, **89**, 106801.
34. Yang, H. *et al*., *Science.* 2012, **336**, 1140-1143.
35. Britnell, L. *et al.*, *Science.* 2012, **335**, 947 – 950.
36. Chung, C. *et al*., *Nano Lett.* 2011, **11**, 1863 – 1867.
37. Yu, Y-J. et *al*., *Nano Lett.* 2009, **9**, 3430 – 3434.
38. Giannozzi, P. *et al., J. Phys.: Condens. Matter.* 2009, **21**, 395502.
39. Perdew, J. *et al*., *Phys. Rev. Lett.* 1996, **77**, 3865.
40. Vanderbilt, D., *Phys. Rev. **B*** 1990, **41**, 7892.
41. Qian, X. et al., *Science* 2014, **346**, 1344.

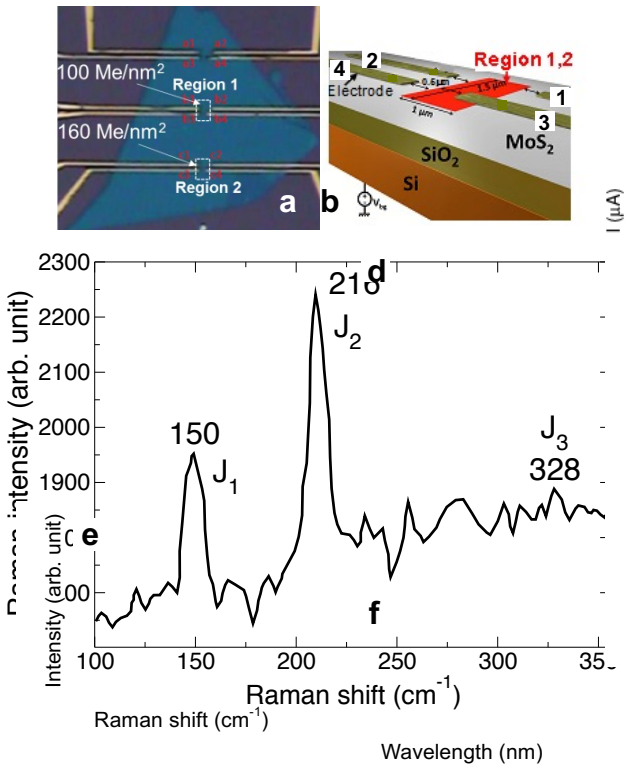

Figure 1

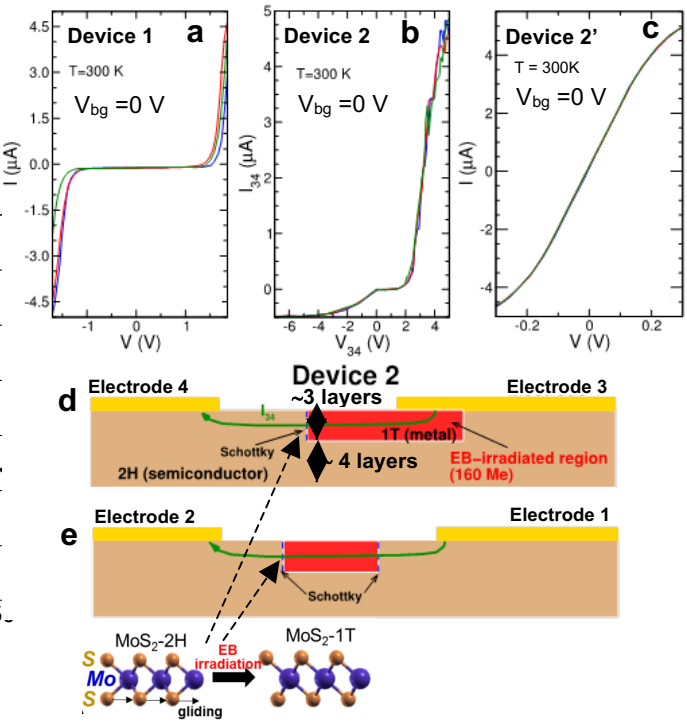

Figure 2

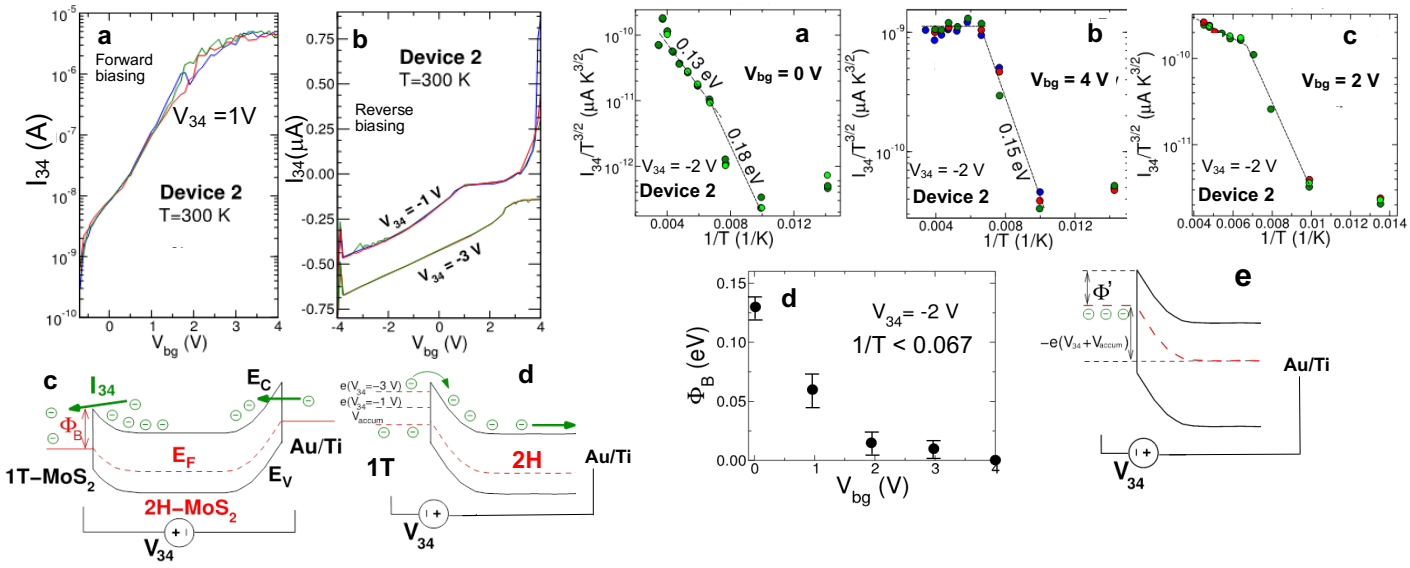

Figure 3

Figure 4

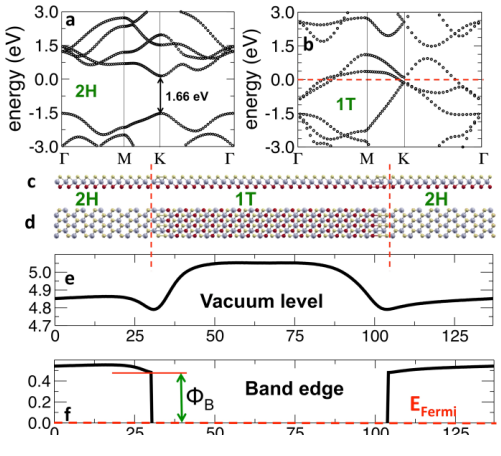

Figure 5

Figure captions

Figure 1. Structural information of few-layer MoS_2 and characterization. **(a)** Optical microscope image of few-layer MoS_2, mechanically exfoliated from bulk, with two EB irradiation regions and two electrode pairs patterned on individual regions. **(b)** Schematic view of an electrode pair on one EB-irradiated region of (a). **(c, d)** XPS spectra of sample shown in (a), which have been measured including the EB-irradiated region 2 and non-irradiated region, showing the Mo 3*d*, S 2*s* (c), and S 2*p* (d) peaks of the 1T phases of MoS_2. Typical experimentally measured spectra are shown in black and fits are shown in red (for the 2H phase component) and blue (for the 1T phase component). **(e)** Typical Raman spectra of EB-irradiated region 2 in (a), showing three peaks unique to the 1T phases of MoS_2. **(f)** PL spectra (via. laser wavelength with 488 nm) of area including region 2 in (a) (see **inset**), exhibiting two absorption peaks due to direct excitonic transitions unique to 2H-MoS_2 (No. 1,2,3) and its complete quench (No.4) on EB non-irradiated and irradiated regions, respectively. **Inset**; PL map with 0.25 μm^2 space resolution, corresponding to wave length of 102 nm (black) ~ 686 nm (red). The number 1-4 correspond to those in main panel.

Figure 2. Room-temperature I vs. V relationships for individual electrode pairs formed around two EB-irradiated regions of Fig. 1(a) for **(a)** Device 1, **(b)** electrode pair 3-4 of Device 2, and **(c)** electrode pair formed on EB-irradiated region with 160 Me/nm^2 in another sample (Device 2'). Results of three-times measurements are shown in different colors on individual figures. **(d, e)** Schematic cross sections of Device 2 for electrode pairs (d) 3-4 and (e) 1-2, corresponding to Fig. 1e. Number of layers of ~4 at bottom-side 2H MoS_2 of EB-irradiated region has been confirmed by Raman peak observed around 407 cm^{-1} (A_{1g} peak). That of ~3 at upper-side 1T MoS_2 has been determined by subtracting the 4 layers from total layer number of 7. **Inset of (e)**: Schematic views of two-different-atomic structured mono-layer MoS_2 crystals; 2H semiconducting and 1T metal phases.

Figure 3. Room-temperature back-gate voltage (V_{bg}) dependence of Fig. 2b (Electrode pair 3-4 in Device 2). **(a, b)** I_{34} vs. V_{bg} relationships for the forward (a) and reverse (b) V_{34}. Y-axis of (a) is a logarithmic. Results of three-time measurements are shown in different colors on individual figures. Note that current limiter of the measurement facility is set to 5 μA through all measurements. **(c, d)** Schematic energy band diagrams of (c) Schottky barrier (SB) FET consisting of (1T-metal)/(2H-semiconductor)/(Ti/Au electrode 3) under forward bias voltage ($+V_{34}$) and $+V_{bg}$, and (d) 1T/2H-phase MoS_2 Schottky junction under reverse bias voltage ($-V_{34}$) and $+V_{bg}$ (see Fig. 2e). In (d), eV_{accm} is the electrostatic energy caused by electron accumulation by applying $+V_{bg}$.

Figure 4. Temperature dependence of I_{34} (Arrhenius plot and 2D Schottky formula) of Fig. 3a and gate tunability. **(a, b)** I_{34} normalized by temperature ($I_{34}/T^{3/2}$) vs. 1/T at V_{bg} = 0V (a) and 4V (b) under fixed V_{34} = -2V. **(c)** that for intermediate V_{bg} = 2V under V_{34}= -2V. Dotted lines are obtained by data fitting using eqs. (1) – (4). **(d)** Gate-tunability of Φ_B, including results of (a) – (c). The error bars show the results of three samples. **(e)** Schematic energy band of 1T/2H-phase MoS_2 Schottky junction under reverse bias voltage ($-V_{34}$) and $+V_{bg}$ to explain (d).

Figure 5 Calculation results based on density functional theory (DFT). **(a)** 2H-MoS_2 monolayer bands. **(b)** 1T-MoS_2 monolayer bands. **(c)** Side and **(d)** top atomistic schematic representation of the 2H/1T/2H MoS_2 heterostructure. **(e)** Vacuum level and **(f)** Band edges of the structure, as computed from DFT calculations. E_F of the hetero-structure has been considered as the reference potential for both potentials shown in **(e)** and **(f)**.